PHYSICAL REVIEW B **79**, 245318 (2009)

Dynamics of electronic transport in a semiconductor superlattice with a shunting side layer

Huidong Xu,[1] Andreas Amann,[2] Eckehard Schöll,[3] and Stephen W. Teitsworth[1]
[1]*Department of Physics, Duke University, P.O. Box 90305, Durham, North Carolina 27708-0305, USA*
[2]*Tyndall National Institute, Lee Maltings, Cork, Ireland*
[3]*Institut für Theoretische Physik, Technische Universität Berlin, Hardenbergstraße 36, 10623 Berlin, Germany*

(Received 18 December 2008; revised manuscript received 27 May 2009; published 19 June 2009)

We study a model describing electronic transport in a weakly coupled semiconductor superlattice with a shunting side layer. Key parameters include the lateral size of the superlattice, the connectivity between the quantum wells of the superlattice and the shunt layer, and the conduction properties of the shunt layer. For a superlattice with small lateral extent and high quality shunt, static electric field domains are *suppressed* and a spatially uniform field configuration is predicted to be stable, results that may be useful for proposed devices such as a superlattice-based terahertz oscillators. As the lateral size of the superlattice increases, the uniform field configuration loses its stability to either static or dynamic field domains regardless of shunt properties. A lower quality shunt generally leads to regular and chaotic current oscillations and complex spatiotemporal dynamics in the field profile. Bifurcations separating static and dynamic behaviors are characterized and found to be dependent on the shunt properties.

DOI: 10.1103/PhysRevB.79.245318 PACS number(s): 73.21.Cd, 72.20.Ht, 05.45.−a

I. INTRODUCTION

Theoretical work by Esaki and Tsu[1] in 1970 was the first to propose a Bloch oscillator based on a superlattice (SL) structure. In that paper, they derived current-voltage (I-V) characteristics of a SL which showed negative differential conductivity (NDC) associated with Bloch oscillations[2,3] of the miniband electrons under a dc bias. However, direct observation of Bloch oscillations is difficult due to decoherence caused by electron scattering. In other important early work, Ktitorov *et al.*[4] predicted a negative high-frequency differential conductivity and associated amplification of high-frequency signals thereby suggesting an alternative means of terahertz oscillation. This dynamic conductivity remains negative up to the Bloch frequency ω_B and reaches a resonance minimum at a frequency closely below ω_B, suggesting that the SL may serve as an active medium for terahertz radiation.

However, no such devices have been realized to date more than three decades after their proposal because the NDC causes space-charge instability. Although Bloch oscillations have been observed experimentally in undoped SLs (Ref. 5) by studying optical dephasing of Wannier-Stark ladder[6] excitations using degenerate four-wave mixing,[7,8] the power of coherent terahertz emission is very small. However, these experiments have shown that the frequency of the emission is tunable by simply changing the applied voltage.[9,10] For high current densities, the space-charge instability causes moving charge accumulation layers (CALs) and charge depletion layers (CDLs) and thus the SL exhibits oscillations similar to the Gunn effect.[11] While devices based on these oscillations may operate in the microwave range, they do not extend to the terahertz region.[12]

The lack of suitable terahertz radiation sources and detectors hampers the technological exploitation of the frequency regime spanning from 300 GHz to 10 THz. Quantum cascade laser devices have been shown to operate in the terahertz range for temperatures up to 164 K.[13] On the other hand, if superlattice-based Bloch oscillators could be successfully realized they might be expected to have certain advantages relative to the quantum cascade structures.[14] Recently, rapid progress in terahertz technology[15] including biomedical sensing, three-dimensional imaging, and chemical agent detection has attracted renewed attention to Bloch oscillators. Some structures have been proposed to stabilize the field in the SL against NDC-related instabilities. One scheme theoretically proposed by Hyart *et al.*[16] is the dc-ac-driven SL which requires the presence of an initial terahertz pump. The SL is biased in the NDC region under a dc electric field, initially superposed with an ac pump electric field which stabilizes the field distribution.[17] Then the initial pump field can be gradually turned off when terahertz oscillation has been already established in the SL. Alternative schemes that do not require a terahertz pump include the use of quasistatically modulated microwave bias[18] or parametric amplification.[19,20] Another suggestion is to stack a few short SLs, where domains are not able to form.[21] These short SLs are separated by heavily doped material, and an increase in terahertz transmission at dc bias has been observed.

Yet another scheme is to open a shunting channel parallel to the SL, similar to a method that has been used to stabilize tunnel diode circuits.[22,23] Daniel *et al.*[24] used a distributed nonlinear circuit model to simulate the electric field domain suppression in a SL. They have shown that the shunt is able to suppress the voltage inhomogeneity above a critical bias voltage which depends on the shunt width, the SL width, and the shunt resistivity. However, the circuit model does not include aspects of the electronic tunneling transport that appear to play an important role in SL behavior. The model possesses only a global coupling since the elements are connected in series and the I-V characteristic of each element is fixed. On the other hand, the SL model has a more complex structure that has both a global coupling due to the applied voltage constraint as well as a nearest-neighbor coupling arising from the varying charge densities that dynamically change the local current density vs field (J-F) characteristics. As a result, the nonlinear circuit model of Daniel *et al.* is not able to exhibit connected field domains or current self-oscillations that are observed in SL structures both theoretically and experimentally.[25]

In similar work by Feil *et al.*,[26] a side layer is grown on the cleaved edge of a lightly doped GaAs/AlGaAs SL, such that a two-dimensional (2D) electron gas is formed at the interface between the SL and the side layer. The lightly doped SL serves two purposes: (i) to provide a modulated potential for the 2D electron gas at the interface so that under this periodic potential, the electron gas becomes a *surface* SL with one lateral dimension; (ii) to provide a uniform field to this surface SL since a lightly doped SL can maintain a uniform field under external bias. While the suppression of field instabilities has been reported in this type of SL, it is still not clear whether this lateral structure will be useful as a terahertz oscillator.

In this paper, we study an extension of a well-established model of electronic transport in weakly coupled superlattices by adding a shunting side layer. Our treatment includes the effect of lateral electronic (i.e., horizontal) transport within each of the quantum well layers. Here, the vertical electron dynamics is associated with sequential resonant tunneling between weakly coupled quantum well layers rather than miniband transport or Wannier-Stark hopping as occurs for strongly coupled SLs. Although the Bloch oscillator generally requires a strongly coupled SL, the weakly coupled SL has similar NDC features in *I-V* characteristics and similar current self-oscillations occur due to recycling of electronic fronts.[14,27] It has previously been shown by a detailed theoretical analysis[25] that weakly coupled and strongly coupled superlattices give similar results for the nonlinear transport properties in the NDC regime (cf. also Refs. 28–30).

In Sec. II, we establish a two-dimensional model for describing the current flow and dynamical electric field profile in a shunted SL. In Sec. III, we discuss the extremely different time scales involved in this model, which are challenges to numerically solving it. In Sec. IV, we numerically explore the effect of a high quality shunt on the dynamics of SLs as the lateral size of the SL is varied and show that the uniform field configuration is stable, provided that the shunt and shunt connection have high enough quality and the SL lateral extent is not too great. In Sec. V, we choose a laterally narrow SL and study the dependence of the SL dynamics on the shunt properties. The transition from a stable uniform field configuration to static field domains is found to be complex and the bifurcations involved in this transition are discussed. The Appendix presents details of the numerical methods employed.

II. LATERALLY EXTENDED MODEL OF THE SUPERLATTICE WITH SHUNT LAYER

Weakly coupled semiconductor superlattices have been successfully described by the sequential resonant tunneling model over the past several years.[25,27,31,32] However, previous works usually consider only the dynamics along the growth (vertical) direction of the SL and ignore the dynamics in the in-plane (lateral) direction, i.e., treat each period as an infinitely large plane with uniform charge density. More recently, Amann and Schöll[33] developed a theoretical framework which describes both lateral and vertical electronic dynamics. Here, we extend this framework to include the effects of a shunting side layer.

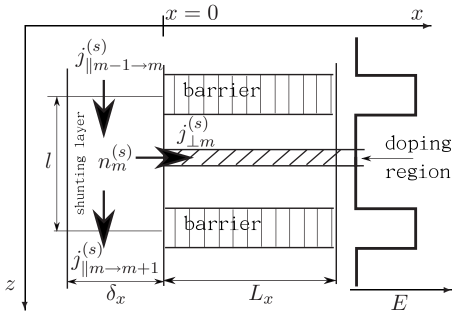

FIG. 1. Schematic of the shunted SL. The growth direction is along the z direction and the quantum wells are parallel to the x direction. The SL is located at $x>0$ and the shunt is at $x<0$. The thick line on the right is the potential energy of an electron in the conduction band of the SL.

The structure of the shunted SL is shown in Fig. 1. Each quantum well forms a slab that is parallel to the x-y plane, with cross sectional dimensions L_x and L_y. There are N such quantum wells stacked on top of each other in the z direction, sandwiched between an emitter layer and a collector layer. The shunt layer is located between $-\delta_x \leq x \leq 0$, with thickness δ_x. The SL period is $l=w+d$, where w and d are the width of the quantum well and width of the barrier, respectively. The external voltage is applied in the z direction across the emitter and the collector.

Inside the SL, the electrons are localized within one quantum well due to the relatively thick quantum barriers. Furthermore, the electrons are assumed to be at local equilibrium and the local *two-dimensional* charge density at time t is denoted by $n_m(x,y,t)$, where m is the well index and x, y are the in-plane coordinates. The charge continuity equation in the SL can be written as

$$e\dot{n}_m(x,y,t) = j_{\parallel m-1\to m} - j_{\parallel m\to m+1} - \nabla_\perp \cdot \mathbf{j}_{\perp m}, \tag{1}$$

where

$$\nabla_\perp = \mathbf{e}_x \frac{\partial}{\partial x} + \mathbf{e}_y \frac{\partial}{\partial y}, \tag{2}$$

$j_{\parallel m-1\to m}$ denotes the three-dimensional vertical current in z direction tunneling through each barrier (units: A/m^2), and $\mathbf{j}_{\perp m}$ is the lateral two-dimensional current density (units: A/m). The electron charge is $e<0$. The y dependence is ignored and Eq. (1) can be rewritten as

$$e\dot{n}_m(x,t) = j_{\parallel m-1\to m} - j_{\parallel m\to m+1} - \frac{\partial j_{\perp m}(x)}{\partial x}. \tag{3}$$

The local vertical tunneling current $j_{\parallel m\to m+1}$ through each barrier is described by the sequential resonant tunneling model which has been derived using different methods;[25,27,32] in this paper, we have used the same form as in Refs. 25 and 32. This tunneling current depends on the electric field $F_{\parallel m}(x)$ across the barrier through which the tunneling occurs and the electron charge densities $n_{m-1}(x)$ and $n_m(x)$ in the neighboring quantum wells of this barrier. Thus, the tunneling current has the functional form

$$j_{\parallel m-1\to m}(x) = j_{\parallel m-1\to m}[F_{\parallel m}(x), n_{m-1}(x), n_m(x)]. \tag{4}$$

If the charge density is uniform, the tunneling current $J_{\parallel}(F, N_D, N_D)$ follows the dashed-dotted curve in Fig. 3(b). The conductivity peak is due to resonant tunneling between nonequivalent levels in adjacent wells. The negative conductivity part is due to nonresonant tunneling of electrons when the applied field across the barrier is high enough such that the ground levels in neighboring quantum wells mismatch. The tunneling current densities through the emitter and collector layers are modeled by Ohmic boundary conditions,[33] that is, $j_{\parallel 0\to 1}(x)=\sigma F_{\parallel 0}(x)$ and $j_{\parallel N\to N+1}(x)=\sigma F_{\parallel N}(x) n_N/N_D$, with contact conductivity σ and two-dimensional doping density N_D in each well.

The lateral dynamics is caused by the in-plane current $\mathbf{j}_{\perp m}$ which consists of a drift part and a diffusion part. When the y dependence is ignored, this becomes

$$j_{\perp m}(x) = -e\mu n_m F_{\perp m} - eD_0\frac{\partial n_m}{\partial x}, \tag{5}$$

where $F_{\perp m}(x)$ is the in-plane component of the electric field at x in well m, μ is the mobility, and D_0 is the diffusion coefficient. The generalized Einstein relation[34] establishes the connection between μ and D_0 for arbitrary two-dimensional electron densities including the degenerate regime,

$$D_0(n_m) = \frac{n_m}{-e\rho_0\{1-\exp[-n_m/(\rho_0 k_B T)]\}}\mu, \tag{6}$$

with the two-dimensional density of states $\rho_0 = m^*/(\pi\hbar^2)$, where m^* is the electron effective mass. Here we assume that μ and D_0 are fixed.

Both the lateral and vertical currents depend on the electrical fields which in turn depend on the scalar potential $\phi_m(x,y)$. The potential can be solved by the Poisson equation

$$\Delta\phi_m(x,y) = (\Delta_\perp + \Delta_\parallel)\phi_m(x,y) = -\frac{e}{l\epsilon_r\epsilon_0}(n_m - N_D), \tag{7}$$

with

$$\Delta_\perp\phi_m(x) = \frac{\partial^2}{\partial x^2}\phi_m(x), \tag{8}$$

$$\Delta_\parallel\phi_m(x) = \frac{\phi_{m-1}(x) - 2\phi_m(x) + \phi_{m+1}(x)}{l^2}, \tag{9}$$

where ϵ_r and ϵ_0 are the relative and absolute permittivities, respectively. Then the field can be calculated as

$$F_{\parallel m}(x,y) = \frac{\phi_{m+1}(x) - \phi_m(x)}{l},$$

$$F_{\perp m}(x) = -\frac{\partial\phi_m(x)}{\partial x}. \tag{10}$$

Here we solve the Poisson equation using an approximation method assuming that the typical structures in the lateral direction vary on a length scale much longer than the mean-free path of the degenerate electrons.[33]

The drift-diffusion dynamics of the shunting layer is similar to that of the lateral dynamics within each SL quantum well. First, we neglect x dependence in the shunt, that is, the shunt is collapsed into a single layer along the z direction. Note also that unlike the SL, which possesses an intrinsic discreteness along z direction, the shunt is a continuous layer. Therefore, we make a further approximation that the shunt is divided into blocks aligned with the periods of the SL and that the charge density is locally uniform within each block. This assumption not only provides the discretization required by numerical simulation but also matches the dynamics of the shunt with that of the SL. With these two assumptions, we can write down the continuity equation in the mth shunt block as follows:

$$e\dot{\tilde{n}}^{(s)}_m(t)\cdot\delta_x l L_y = j^{(s)}_{\parallel m-1\to m}\cdot\delta_x L_y - j^{(s)}_{\parallel m\to m+1}\cdot\delta_x L_y - \tilde{j}^{(s)}_{\perp m}\cdot l L_y, \tag{11}$$

where the superscript (s) denotes the quantities in the shunt and the tilde denotes that the quantities are three-dimensional, i.e.,

$$n^{(s)}_m = \tilde{n}^{(s)}_m\cdot l, \quad j^{(s)}_{\perp m} = \tilde{j}^{(s)}_{\perp m}\cdot l. \tag{12}$$

Here, the quantity $j^{(s)}_{\perp m}$ denotes the lateral current that flows between the shunt and the SL through their interface. Then we can write Eq. (11) in the form

$$e\dot{n}^{(s)}_m(t) = j^{(s)}_{\parallel m-1\to m} - j^{(s)}_{\parallel m\to m+1} - \frac{j^{(s)}_{\perp m}}{\delta_x}. \tag{13}$$

Note that the vertical current in the shunt has a very different form than the tunneling current in the SL. It follows a similar dynamics as the in-plane current in the SL quantum wells and is related to the three-dimensional charge density in the shunt,

$$j^{(s)}_{\parallel m-1\to m} = -e\mu\tilde{n}^{(s)}_m F^{(s)}_{\parallel m} - eD_0\frac{\partial\tilde{n}^{(s)}_m}{\partial z}. \tag{14}$$

Here we assume the mobility μ and the diffusion coefficient D_0 have the same values as in the SL.

Next, we examine the lateral current that connects the shunt and the quantum well layer within the SL,

$$j^{(s)}_{\perp m} = -e\mu n_m(x=0)F_{\perp m} - D_0\nabla_\perp n_m|_{x=0^+}. \tag{15}$$

In this equation, the boundary should be defined at $x=0^+$ for calculation of both the current and the potential in the shunt. Since the shunt is assumed to be uniform in x direction, defining the above equation at $x=0^-$ implies that $F_{\perp m}$ and $\nabla_\perp n^{(s)}_m$ are zero which would lead to zero boundary current. Another advantage of choosing the boundary at $x=0^+$ is that the potential in the shunt should be equal to the potential in the SL close to its boundary, i.e., $\phi^{(s)}_m(x<0)=\phi_m(x=0^+)$, since the potential is continuous everywhere. This relation allows us to equate the potential in the shunt with that at the inner boundary of the SL. So the potential at the boundary of the solution of Eq. (7) is just the potential in the shunt. The fields required to calculate the current in Eq. (15) can be obtained by

$$F^{(s)}_{\|m}(x) = \frac{\phi^{(s)}_{m+1}(x) - \phi^{(s)}_m(x)}{l},$$

$$F_{\perp m}(0^+) = -\nabla_\perp \phi_m(x)|_{x=0^+}. \tag{16}$$

The charge density and its normal gradient at the boundary are

$$n_m(x=0) = \frac{n_m(0^+) + n^{(s)}_m(0^-)}{2}, \tag{17}$$

$$\nabla_\perp n_m|_{x=0^+} = \lim_{\Delta x \to 0^+} \frac{n_m(\Delta x) - n^{(s)}_m}{\Delta x}. \tag{18}$$

Here we also note the possible effects of energy band structure of the shunted SL and the doping density in the shunt. In the above discussion, the situation has been simplified because no band bending is included. However, variations in doping densities in the shunt and the SL can cause band bending effects at the interface. Even if the shunt is doped to have the same Fermi level as that in the SL so that little band bending might be expected, there are other issues that impact the connection quality between the shunt and the SL, for example, surface roughness and the presence of trap states or a thin oxide layer. On the other hand, these effects can be minimized through the use of a fabrication process such as cleaved edge overgrowth which is known to produce very high quality interfaces.[35,36] To quantify the quality of the connection between the SL and the shunt, we introduce a parameter $0 \le a \le 1$ such that $a=1$ corresponds to a perfect connection and $a=0$ corresponds to no connection. This leads to the following modification of Eq. (15):

$$j^{(s)}_{\perp m} = a \cdot [-e\mu n_m(x=0) F_{\perp m} - D_0 \nabla_\perp n_m|_{x=0^+}]. \tag{19}$$

Here we note that the determination of a values for specific interface types would be a separate theoretical or experimental work which is beyond the scope of the present paper.

Similarly, we introduce a separate parameter $b > 0$ that allows us to model the effect of having different doping densities and/or mobilities in the shunt vs SL quantum wells. Also, recognize that the field in the shunt is almost uniform and $n^{(s)}_m \approx N^{(s)}_D$ when the conductance in the shunt is high, where $N^{(s)}_D$ is the doping density in the shunt. This leads to the following modification of Eq. (14):

$$j^{(s)}_{\|m-1\to m} = -e\mu \tilde{n}^{(s)}_m F^{(s)}_{\|m} - eD_0 \frac{\partial \tilde{n}^{(s)}_m}{\partial z} \approx -eb\mu^{(s)} \tilde{N}_D F^{(s)}_{\|m}, \tag{20}$$

where $b\mu\tilde{N}_D = \mu^{(s)}\tilde{N}^{(s)}_D$. Note that $b > 1$ when the doping density in the shunt is greater than that in the quantum wells and b is much less than one when the shunt is weakly conducting so that only a small fraction of the total vertical current flows through it.

It is also useful to point out that the total current,

$$J = (\epsilon_r \epsilon_0 \dot{F}^{(s)}_{\|m} + j^{(s)}_{\|m\to m+1}) \cdot \delta_x + \int_0^{L_x} (\epsilon_r \epsilon_0 \dot{F}_{\|m} + j_{\|m\to m+1}) dx, \tag{21}$$

is the same for each period. To show this, note that the Poisson equation can be written as

$$\nabla \cdot (\mathbf{F}_\perp + \mathbf{F}_\|) = \frac{e}{l\epsilon_r \epsilon_0}(n_m - N_D) \tag{22}$$

or

$$\frac{F_{\|m} - F_{\|m-1}}{l} + \frac{\partial F_\perp}{\partial x} = \frac{e}{l\epsilon_r \epsilon_0}(n_m - N_D). \tag{23}$$

Substituting the above equation into Eq. (3) yields

$$l\epsilon_r \epsilon_0 \frac{d}{dt}\left(\frac{F_{\|m} - F_{\|m-1}}{l} + \frac{\partial F_\perp}{\partial x}\right) = j_{\|m-1\to m} - j_{\|m\to m+1} - \frac{\partial j_{\perp m}(x)}{\partial x}. \tag{24}$$

Then, one integrates both sides of the preceeding equation with respect to x from $-\delta_x$ to L_x. Due to the vanishing boundary conditions $F_\perp(-\delta_x) = F_\perp(L_x) = 0$ and $j_{\perp m}(-\delta_x) = j_{\perp m}(L_x) = 0$, the lateral terms in the above equation integrate to zero. This yields

$$\epsilon_r \epsilon_0 \frac{d}{dt}\int_{-\delta_x}^{L_x} F_{\|m} dx + \int_{-\delta_x}^{L_x} j_{\|m\to m+1} dx = \epsilon_r \epsilon_0 \frac{d}{dt}\int_{-\delta_x}^{L_x} F_{\|m-1} dx + \int_{-\delta_x}^{L_x} j_{\|m-1\to m} dx, \tag{25}$$

which shows that the total current is independent of the well index m. Note that the current through the shunt will be the dominating contribution to the total current of a SL if the shunt is thick and well conducting. Even a completely disconnected shunt (i.e., $a=0$) contributes a constant current of $J^{(s)}_0 = \delta_x e\mu N_D U/(Nl+d)$ to the total current J of a homogeneous SL. Since we are interested in effects arising from the interaction between the SL and the shunt, we will in the following discuss the current dynamics on the basis of the SL current defined by $J_{\mathrm{SL}}(t) = J(t) - J^{(s)}_0$.

III. PARAMETERS AND TIME SCALES

The parameters that we use in the simulation are listed in Table I. These parameters come from weakly coupled GaAs/AlAs superlattice structures that have been studied in experiments.[37] Variations in the parameters such as barrier thickness and doping density have been extensively studied in previous work and dynamical features are found to be robust.[25] The nonlinear behaviors such as current branches are clearly seen at low temperature in experiments.[38] The quantum wells and the shunt are GaAs with same doping level and the barriers are undoped AlAs. We make the as-

TABLE I. Parameters used for the shunted SL.

N	N_D (m^{-2})	w (nm)	d (nm)	μ ($\mathrm{m}^2/\mathrm{V\ s}$)	D_0 (m^2/s)	T (K)	ϵ_r
40	1.5×10^{15}	9	4	10	0.015	5	13.18

sumption that mobility μ and D_0 are fixed and choose typical values for GaAs.[33] We expect qualitative agreement over a large parameter regime. We found that there are very different time scales in this complex structure which requires an implicit method of numerical iteration. The first time scale τ_b is the dielectric relaxation time in the bulk material both in the shunt and in each quantum well in the SL. It is determined by the doping density. We know that the conductivity g is proportional to the charge density

$$g \approx e\mu N_D/l \sim 1.6\times10^{-19}\times10\times10^{23}\ (\Omega\ \mathrm{m})^{-1} \sim 10^5\ (\Omega\ \mathrm{m})^{-1}. \qquad (26)$$

So the dielectric relaxation time in the shunt layer and within each quantum well is approximated as

$$\tau_b = \frac{\epsilon_r\epsilon_0}{g} \sim \frac{0.1\times10^{-9}}{10^5}\ (\mathrm{s}) \sim 10^{-15}\ \mathrm{s}, \qquad (27)$$

which is relatively fast due to the high conductivity. This is the time it takes for a fluctuation in the charge density to be neutralized within either the shunt layer or quantum wells.

The second time scale τ_t is the one in the vertical dynamics. According to the sequential resonant tunneling model, the vertical current is on the order of $10^{-4}\ \mathrm{A/m^2}$ and the positive differential conductivity g_t is on the order of $0.1\ (\Omega\ \mathrm{m})^{-1}$. Thus, $\tau_t=\epsilon_r\epsilon_0/g_t\sim10^{-9}$ s, a much larger time scale than τ_b. Moreover, from numerous previous works, we also know that the behavior of the electrons in the vertical direction is not simply dielectric relaxation. More complex phenomena, such as current self-oscillation or injected dipole relocation due to switching, have much longer time scales ranging up to microseconds. The time scale τ_t sets a lower limit of the time scales for these nonlinear processes.

Another important time scale τ_i is the time that it takes to carry away or supply the electrons in the SL through the shunt. Because the vertical processes are relatively slow, if the shunt has good connection and high conductance, the electrons will move laterally, pass through the intersection between the quantum well and the shunt, and drift away through the shunt. This time scale τ_i is considerably larger than τ_b since the electrons have to move into the shunt first. Later we will see that it takes 1 ns to deplete a full CAL in a small SL. The presence of extremely different time scales means that the numerical integration is a stiff problem and this suggests the use of an implicit method. The numerical procedure is described in the Appendix.

IV. DEPENDENCE OF SHUNTING DYNAMICS ON THE LATERAL SIZE OF THE SUPERLATTICE

In this section, we discuss the effects of the lateral size L_x of the SL with a high quality shunting layer, i.e., $a=b=1$. The shunting layer has a width δ_x such that varying δ_x does not affect the dynamics in the shunt. This is numerically confirmed even for the chaotic case that we will discuss below, where an 80 nm shunting layer has the same effect as an 8 mm one. This is because τ_b is much smaller than τ_i and the electrons entering the shunt are carried away so fast that a change in the shunt conductance does not change τ_i. We will study the SLs with a relatively high contact conductivity $\sigma=0.04\ (\Omega\ \mathrm{m})^{-1}$. At this value of σ, without a shunt, the SL has a static high field domain near the emitter and a static low field domain near the collector separated by a static CAL. Due to the high quality shunt the total current is dominated by the contribution of the current through the shunt. As discussed at the end of Sec. II, we will therefore consider the SL current J_{SL}. Also, since we are varying L_x, we scale current to current density.

A. High quality shunting layer with small L_x

Figure 2 shows charge and current density plots for a relatively narrow SL with lateral extent $L_x=20\ \mu$m. The initial state is prepared as a charge configuration for the SL without shunt at total applied voltage $U=2.1$ V and shows a static charge accumulation layer at the 20th period. After an interval of about 1 ns, the space-charge configuration is almost uniform. The in-plane current is plotted as a vector field and shows that the electrons in the CAL move in the lateral direction (the opposite direction of the current) into the shunt. We can see that when the system reaches steady state, the net charge is almost neutral, i.e., $n=N_D$, everywhere in the SL and the shunt. There are still some small lateral current flows at the first and the last periods.

If we take a close look at the steady state, we find that there is a small CAL at the first period and a CDL nearby [Fig. 3(a)]. The situation is almost inverted near the collector. To better understand this, we focus on the operation points near the emitter shown in Fig. 3(b) at $x=20\ \mu$m. In this case, the field is almost uniform in the SL and each period is biased in the NDC region. The field across the first barrier between the emitter and the first well will also have this same value in the absence of charge accumulation in the first well. This causes a vertical current from the emitter to the first period [thin solid line in Fig. 3(b)] which is much larger than the vertical current in the corresponding NDC region of the SL. Close to the shunt this extra current will give rise to a lateral current which will quickly reach the shunt and is carried away by the shunt. A little further away from the shunt where the lateral current is not sufficient to completely neutralize this extra current, a small CAL is formed in the first well which lowers the electric field and therefore the current across the first barrier. At the same time, the electric field in the second barrier is pushed above the uniform field,

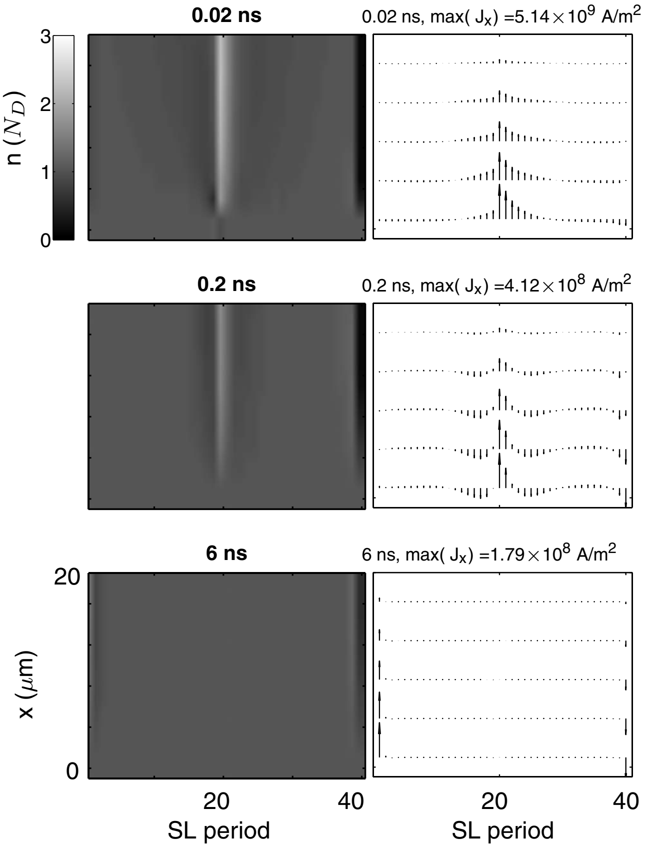

FIG. 2. Charge density plots (left column) and current vector plots of $j_{\perp m}(x)$ (right column) for a SL with $L_x=20$ μm, $U=2.1$ V, and $\sigma=0.04$ $(\Omega\ \text{m})^{-1}$ at 0.02, 0.2, and 6 ns. Initial condition is a CAL at the center of the SL. The shunt is at the bottom. The color bar on the left of the first contour plot is the scale encoding in units of N_D used throughout the paper.

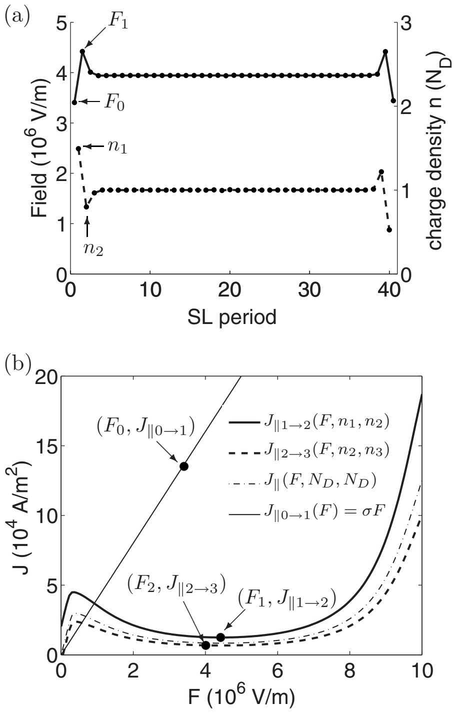

FIG. 3. The steady state for a SL with $L_x=20$ μm, $U=2.1$ V, and $\sigma=0.04$ $(\Omega\ \text{m})^{-1}$ at $x=L_x$: (a) field profile (solid line) and charge density (dashed line); (b) the solid dots indicate the actual current operation points on the local vertical current field characteristics $j_{\|m\to m+1}(F,n_m,n_{m+1})$.

causing a very small CDL next to the CAL. Similar arguments can be applied to the collector to explain the appearance of a small CDL in the last quantum well. The overall effect is that a nearly uniform vertical electric field configuration is stabilized for these conditions.

B. High quality shunting layer with large L_x

As the lateral size L_x of the SL becomes larger, the CAL and CDL near the emitter become more prominent [cf. Figs. 4(a)–4(c), $L_x=160$ μm] since with increasing distance to the shunt the lateral current becomes less efficient at carrying away the excess current from the emitter to the shunt.

For wider SL [cf. Figs. 4(d)–4(f), $L_x=640$ μm], the field closer to the shunt is more uniform and the CAL is still attached to the emitter. However, away from the shunt, the CAL detaches from the emitter and locates itself in the first few periods and the nonuniform field region becomes larger. This behavior is due to the lateral current being insufficient to carry away the extra current from the emitter. Thus, the CAL grows bigger and tends to move toward the collector. With the center of the CAL located in different wells at different x positions, the lateral gradients can be increased and a sufficient lateral current can be sustained. The field profile at $x=640$ μm is plotted in Fig. 4(f). Field domains are forming as the field is low to the left of the CAL and high to the right of the depletion region. In this case, the upstream CAL [closer to the emitter, at the left bottom corner of Fig. 4(d)] and the downstream CAL [closer to the collector, the wider one in Fig. 4(d)] are still connected and this is a time-independent steady state.

In the above case, the lateral size of the SL is just below a characteristic value for which the steady state loses stability to oscillatory behavior. Figure 5 ($L_x=800$ μm) shows the simulations of a slightly wider SL than considered above. The large downstream CAL still stays in that position. However, due to the large size of the SL, the lateral current does not able to sustain a connected stable CAL. The small upstream CAL touches and breaks off from the downstream CAL periodically. There is a small amplitude oscillation in the total current which is shown in the top panel.

For an even wider SL (Fig. 6 with $L_x=1.28$ mm), the upstream and downstream CALs are mostly disconnected. The upstream CAL extends laterally into the SL and moves toward the downstream CAL (at time 1.969 ms). For certain times during the dynamical evolution (not shown in Fig. 6), the upstream CAL breaks off from the emitter and reaches and merges with the downstream CAL. Mostly, there is a depletion region forming between the upstream and downstream CALs (2.211 ms). For certain times, it grows into a full CDL extending across the entire lateral dimension of the structure and, in this case, the upstream CAL also grows into a full CAL (2.395 ms). Then all three fronts begin to move downstream. The downstream CAL and the CDL quickly

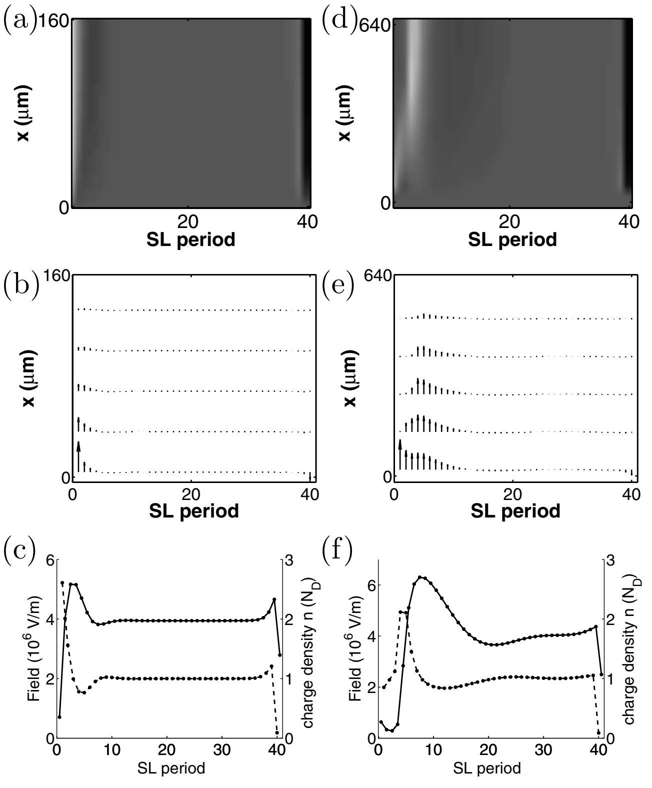

FIG. 4. Steady states: [(a) and (d)] charge density plots, [(b) and (e)] current vector plots, and [(c) and (f)] field profile (solid line) and charge density (dashed line) at $x=L_x$ for $L_x=160$ μm (left column) and $L_x=640$ μm (right column), respectively, with $U=2.1$ V and $\sigma=0.04$ $(\Omega\ \mathrm{m})^{-1}$.

dissipate and the upstream CAL splits into two segments separated by a small CDL, and we return to the situation shown in the leftmost contour plot of Fig. 6. Although these behaviors are quite complicated, they are still periodic, and during each period, the upstream and downstream CALs merge several times.

However, for an extremely wide SL (Fig. 7, $L_x=2.56$ mm), the behavior is apparently chaotic. The effect of the shunt is to cause a CAL attached to the emitter near the shunt. For large values of x, the shunt has less effect and this CAL detaches from the emitter tends to move downstream to the collector and thus extends toward the downstream CAL. Due to the large lateral size of the SL, the impact of the shunt layer becomes very weak on the opposite side of the SL. Thus, the downstream CAL is located very close to the 20th period where it would be in the absence of a shunting layer. The merging of the CALs described in last paragraph also appears here except that the merging events are now difficult to predict and manifestly not periodic.

Figure 8 shows the behavior of a SL with $L_x=5.12$ mm. It should be noted that real SL samples rarely have such a large size. In this case, the unstable dynamics only occurs in the portion of the SL closest to the shunt. In the portion of the SL away from the shunt, a CAL is located at the 20th well, where the shunt has no apparent influence. Over time, the lateral extension of this CAL changes. When a large CDL collides with it at 5.696 ms, the static CAL shrinks to a small size, causing a large dip in the current trace. The presence of such charge tripole configurations[39] of one CDL and two CALs has already been shown to be associated with chaotic behavior in one-dimensional SL models without lateral dynamics.[40]

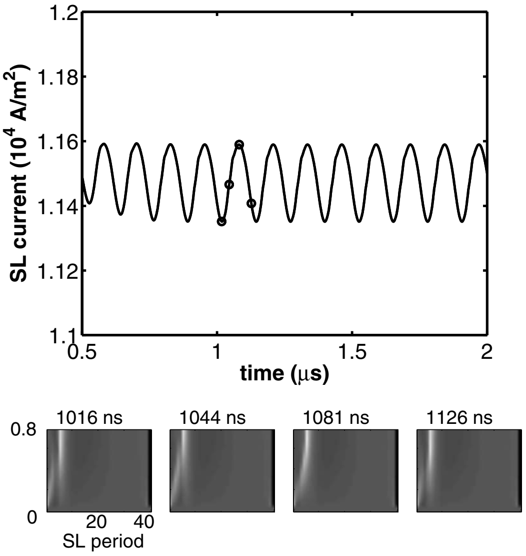

FIG. 5. SL current density J_{SL}/L_x and snapshots of charge density distribution for $L_x=0.8$ mm, $U=2.1$ V, and $\sigma=0.04$ $(\Omega\ \mathrm{m})^{-1}$. The times of the snapshots are marked as solid circles in the upper panel. The contour plots have the same SL period labeling as the first panel.

To summarize, we are able to identify three characteristic length scales in the x direction. The shortest one is the decay length $\bar{L}_x$ (of order 10 μm) at which the charge density in the first quantum well increases from N_D at the SL-shunt interface to its maximum value [cf. Figs. 4(a)–4(c)]. The

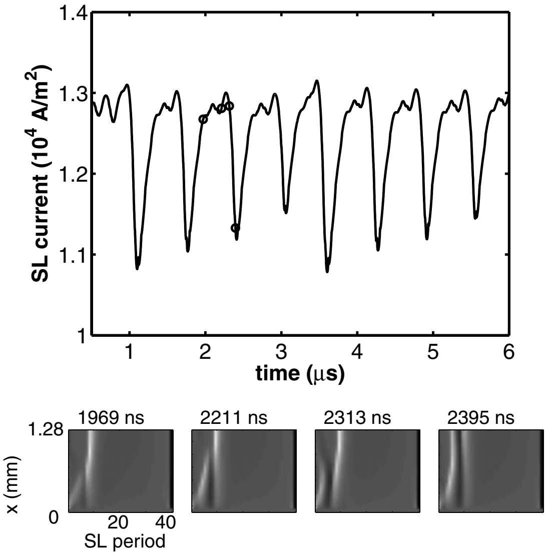

FIG. 6. SL current density J_{SL}/L_x and snapshots of charge density distribution for $L_x=1.28$ mm, $U=2.1$ V, and $\sigma=0.04$ $(\Omega\ \mathrm{m})^{-1}$. The times of the snapshots are marked as solid circles in the upper panel. All the contour plots have the same SL period labeling as the first panel of Fig. 5.

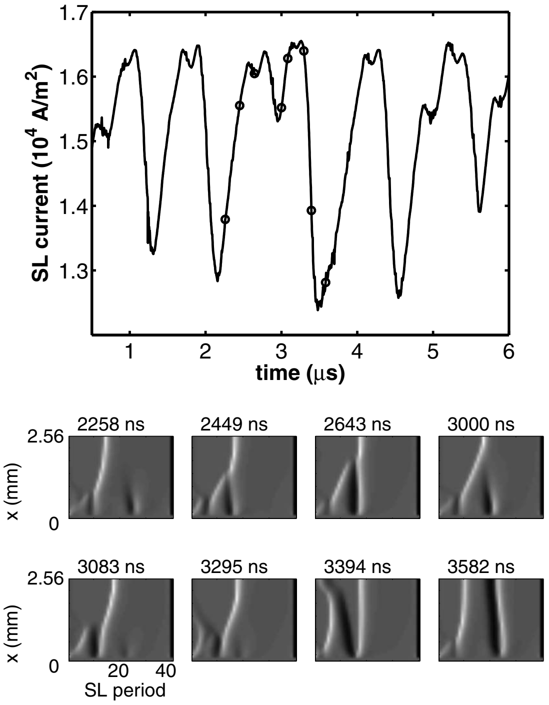

FIG. 7. SL current density J_{SL}/L_x and snapshots of charge density distribution for L_x=2.56 mm, U=2.1 V, and σ =0.04 $(\Omega\ \mathrm{m})^{-1}$. The times of the snapshots are marked as solid circles in the upper panel. All the contour plots have the same SL period labeling as the first panel of Fig. 5.

next length scale (of order 200 μm) is the range above which the vertical field configuration loses uniformity and static field domains start to form [cf. Figs. 4(d)–4(f)]. The longest length scale (of order 700 μm) is the width of the SL above which the steady state loses stability to oscillatory behavior. This implies that lateral uniformity in the electric field distribution can be expected when L_x is smaller than the intermediate characteristic length scale. The shortest decay length $\bar{L}_x$ can be estimated by noting that the extra current coming from the emitter must be directed to the shunt by the negative gradient of the lateral current $J_\perp$, i.e., $\frac{\partial J_\perp(x)}{\partial x}$ $=J_{\|0\to 1}(x)-J_{\|1\to 2}(x)<0$. Then there is approximately a decay length $\bar{L}_x$ at which the quantities such as $J_\perp(x)$, $n(x)$, and $F_x(x)$ approach asymptotic values exponentially. Calculation shows that $\bar{L}_x$ is on order 10 μm for the parameters used in Table I,[41] in agreement with our numerical results.

V. DEPENDENCE OF DYNAMICAL BEHAVIOR ON THE SHUNT PROPERTIES

In Sec. IV B, we have seen that the width of the SL determines the lateral dynamics of electronic transport and that the shunt can stabilize a nearly *uniform* field configuration in sufficiently narrow SLs. Now we investigate the effects of the shunt properties on a small SL with width of 20 μm where the lateral field and electron density profiles are almost uniform. Since the charge density is almost uniform laterally, we modify the model such that *the SL is collapsed to one point in x* direction. This modification significantly reduces the complexity of the simulation. We first study the effects of connectivity parameter a on a SL with conductivity σ=0.04 $(\Omega\ \mathrm{m})^{-1}$ chosen as in Sec. IV B. Then we study the effects of a on a SL with lower contact conductivity σ =0.016 $(\Omega\ \mathrm{m})^{-1}$, which corresponds to moving fronts and current self-oscillations in unshunted SLs,[32] and briefly discuss the effects of shunt conductivity parameter b and width δ_x. The calculation results from this reduced SL model have been confirmed by the full SL model for a range of different values of a. Since L_x is fixed, we plot the unscaled SL current J_{SL}.

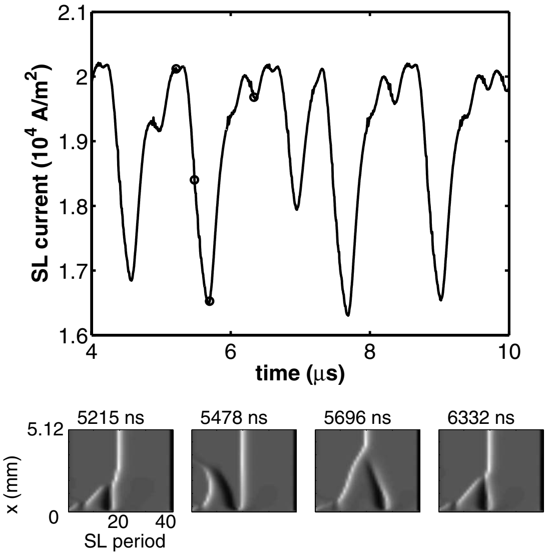

FIG. 8. SL current density J_{SL}/L_x and snapshots of charge density distribution for L_x=5.12 mm, U=2.1 V, and σ =0.04 $(\Omega\ \mathrm{m})^{-1}$. The times of the snapshots are marked as solid circles in the upper panel. All the contour plots have the same SL period labeling as the first panel of Fig. 5.

A. Dynamical behavior vs connectivity parameter *a* for large contact conductivity

Figure 9(a) shows a bifurcation diagram using as the bifurcation parameters the connectivity parameter a and the voltage U for σ=0.04 $(\Omega\ \mathrm{m})^{-1}$. There is a bounded region where the system exhibits periodic or chaotic oscillations, shown as the region enclosed by dashed lines in Fig. 9(a). The value of the connectivity parameter a of the oscillatory region ranges from about 6×10^{-3} to 7×10^{-6}. In real samples, such a weak connection between the SL and the shunt could be associated with a potential barrier formed between the SL and the shunt due to band bending or an oxide layer.

For $a\gtrsim 6\times 10^{-3}$, the charge density in the SL is almost uniform except for a small CDL near the emitter, the same situation shown in Fig. 2. With the increase in voltage, this CDL becomes more prominent and there is a CAL in the first period. However, this CAL never detaches from the emitter for any value of voltage when $a\gtrsim 6\times 10^{-3}$. This is reasonable because for $a\gtrsim 6\times 10^{-3}$, the connection is strong

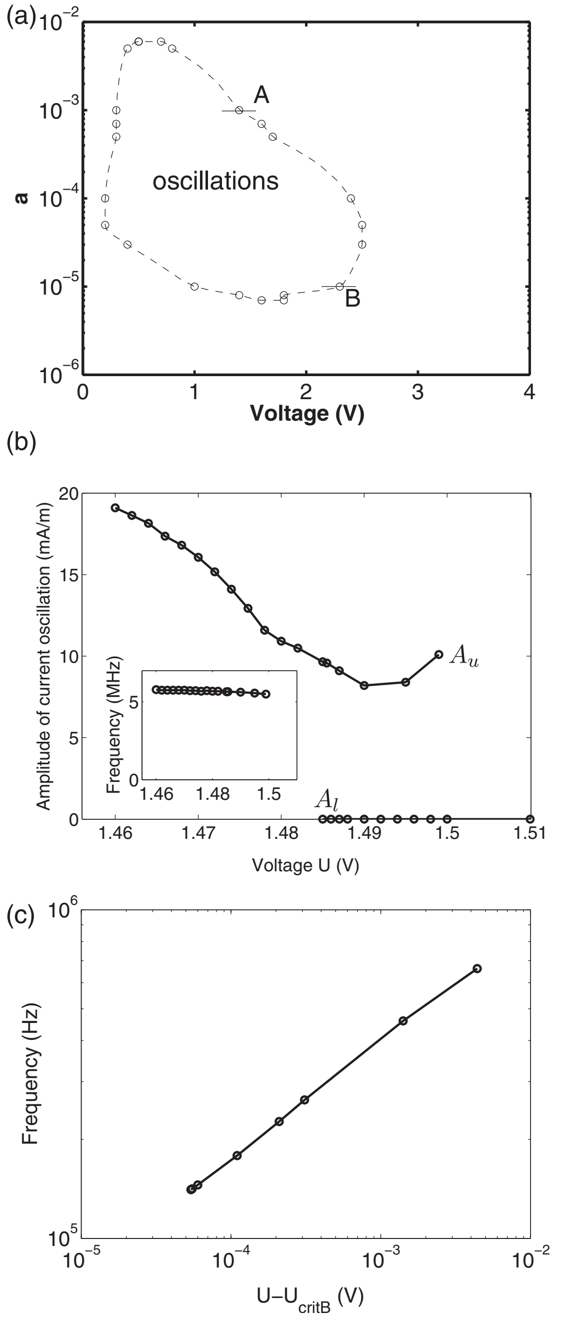

FIG. 9. (a) Bifurcation diagram for $\sigma=0.04\ (\Omega\ \mathrm{m})^{-1}$, $L_x=20\ \mu\mathrm{m}$, and $b=1.00$. Dashed curve shows the approximate boundary of the oscillatory region and location of studied bifurcation points A and B. (b) Bifurcation scenario at A for $a=1.00\times10^{-3}$: amplitude vs voltage (main figure) and frequency vs voltage (inset). Points A_u and A_l denote the end points of the upper and the lower branches, respectively. (c) Bifurcation scenario at B for $a=1.00\times10^{-5}$: scaling of frequency vs voltage (double logarithmic plot); $U_{\mathrm{crit}B}=2.304\,41$ V.

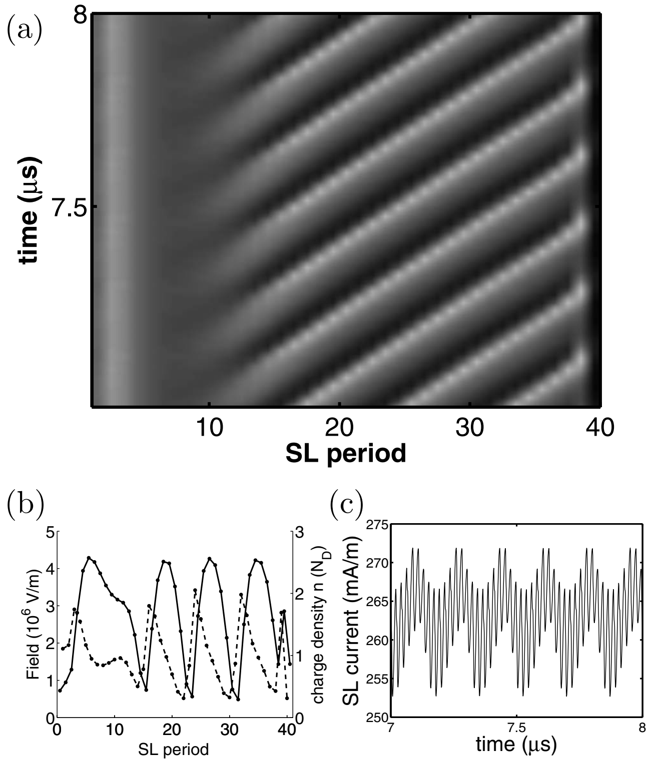

FIG. 10. (a) Charge density distribution evolving in time (gray scale is the same as in Fig. 2), (b) a snapshot of field profile (solid line) and charge density profile (dashed line) at $t=8$ ns, and (c) SL current J_{SL} on the upper branch of Fig. 9(b). Parameters: $a=1.00\times10^{-3}$, $U=1.46$ V, and $\sigma=0.04\ (\Omega\ \mathrm{m})^{-1}$.

enough that the shunt is able to maintain the field in the SL almost uniform.

Another stable region is $a\lesssim7\times10^{-6}$. In this region, a static CAL is formed in the SL and located close to the position where it is expected when there is no shunt. This is also easy to understand because the connection is so weak that the shunt has almost no influence on the SL.

Between these two values of a, we have a transition region where oscillations occur for certain ranges of applied voltage. Here, the bifurcation scenarios by varying voltage are investigated for two sets of values (A and B) of the control parameters.

The bifurcation for point A occurs at $a=1.00\times10^{-3}$ and $U=1.485$ V [Figs. 9(b) and 10–12]. Inside the oscillatory region (approximately $U\leq1.485$ V), the charge density distribution in the SL oscillates and the oscillation only involves part of the SL (cf. Fig. 10). There is a static CAL near the emitter but this is clearly detached from the emitter. The oscillation occurs in the wide region to the right of the CAL in the form of moving charge dipoles (CALs and CDLs) [cf. Fig. 10(a)]. However, at any given time, there are three to four pairs of dipoles present. From Fig. 10(b), we can see that the charge densities have large amplitude fluctuations along the z direction and the higher frequency component of the current oscillation is due to the movement of these dipoles [Fig. 10(c)]. This higher frequency f_1 is nine times the lower one f_2 at which the collector receives the moving dipoles. Here we observe the *coexistence* of static CAL and steady moving fronts.

The bifurcation scenario of A is illustrated by Fig. 9(b), where the amplitude of the current oscillation is plotted versus the applied voltage. There is a bistability region between $U\approx1.485$ and 1.50 V, where the system either oscillates (upper branch) or is in a steady state (lower branch).

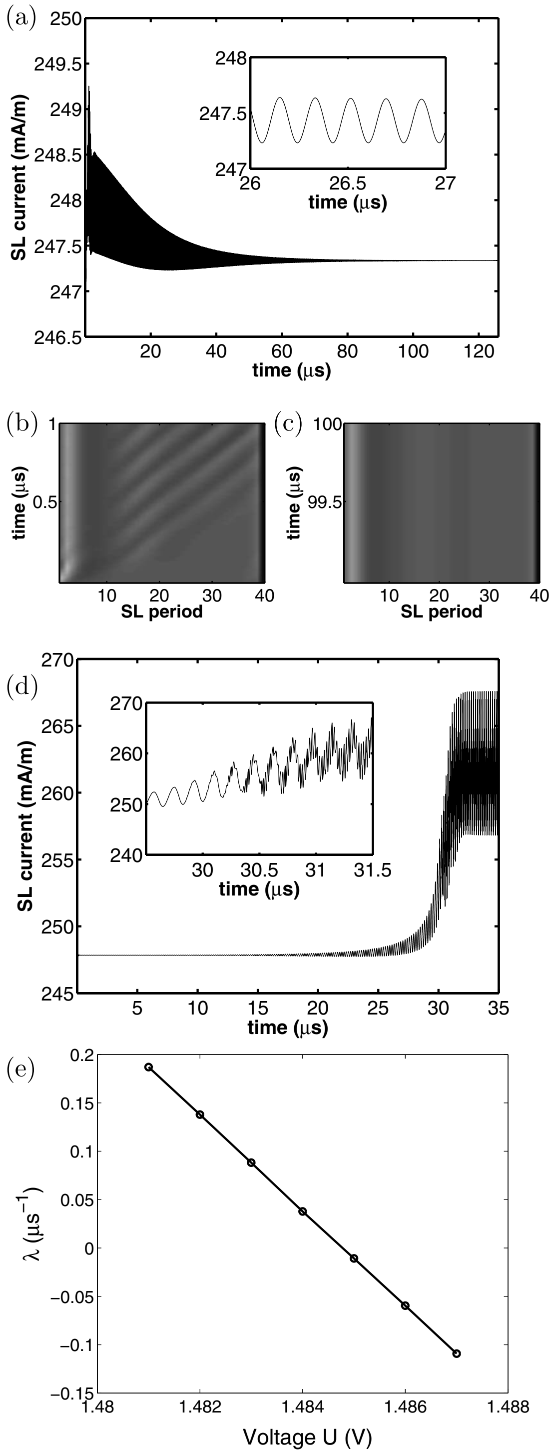

FIG. 11. (a) SL current J_{SL} vs time for $U=1.486$ V (the inset shows an enlargement); [(b) and (c)] charge density distributions evolving for two different time intervals for voltage near bifurcation point A_l. (d) SL current for $U=1.481$ V. (e) The rate λ of exponential decay $\lambda<0$ (or increase $\lambda>0$) of oscillation amplitude versus applied voltage U. Parameters: $a=1.00\times10^{-3}$, $\sigma=0.04$ $(\Omega\ \mathrm{m})^{-1}$.

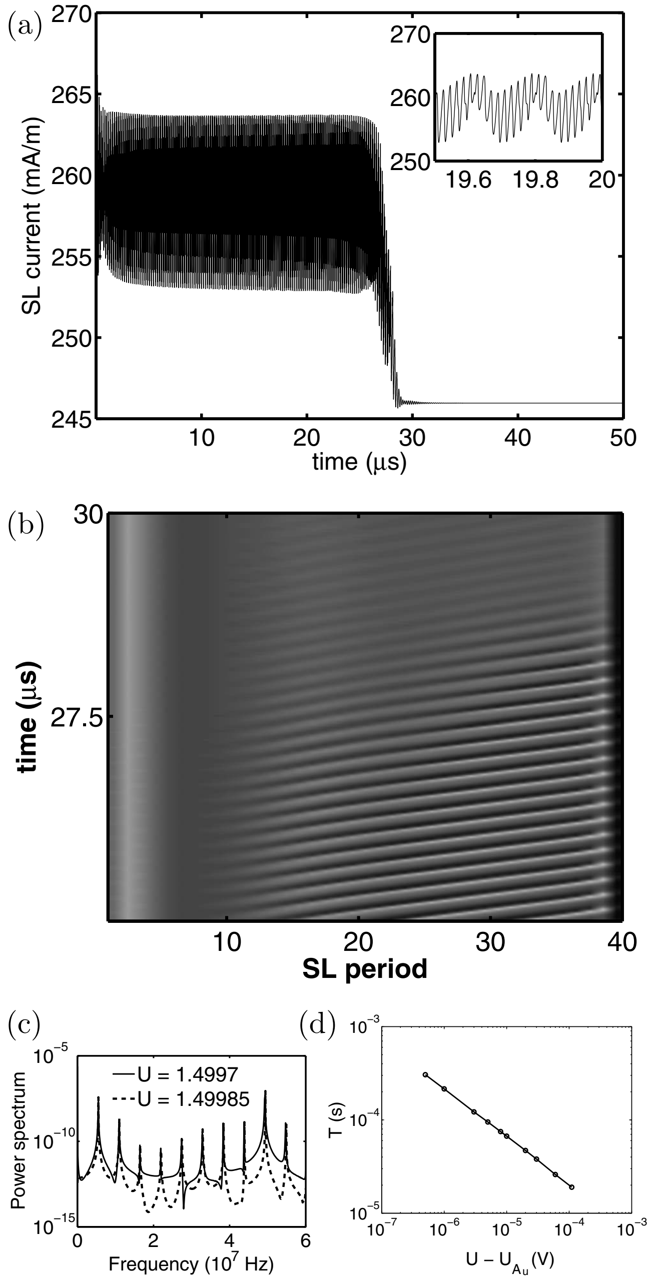

FIG. 12. (a) SL current J_{SL} (the inset shows an enlargement) and (b) charge density distribution evolving in time for $U=1.499\,85$ V with $a=1.00\times10^{-3}$, $\sigma=0.04$ $(\Omega\ \mathrm{m})^{-1}$. (c) Power spectrum data for oscillations at $U=1.4997$ V and $U=1.499\,85$ V. (d) The time T for which the system exhibits transient oscillations versus the applied voltage $U-U_{A_u}$, with $U_{A_u}=1.499\,791$ V.

The bifurcation at point A_l at the end of the lower branch is studied in Fig. 11. When the system starts from a uniform configuration at $U=1.486$ V, shown in Figs. 11(a)–11(c), it first oscillates similar to the full oscillation in Fig. 10, except that the CALs and CDLs are much smaller in Fig. 11(b). The oscillation gradually decays to a steady state where there is only a single stable CAL and no charge fronts to its right, as shown in Fig. 11(c). The amplitude of the current oscillation is quite small and decays to zero. The well-to-well hopping of the small charge fronts does not have an appreciable effect on the current oscillation form as found for the mature fronts in Fig. 10(c). Instead, the shape of the current oscillation is smooth and sinusoidal and possesses a well-defined frequency. After a transient interval, the amplitude $A(t)$ of the current oscillation decays exponentially, i.e., $A(t) = A(t_0)\exp \lambda t$ and the rate λ can be determined by fitting. It also should be mentioned that the initial state corresponding to the uniform field configuration falls into the basin of attraction of the upper oscillatory branch for $U \lesssim 1.486$ V. Hence, to obtain λ for the lower branch, we start the system from the steady state of $U = 1.486$ V. This initial state is used for all the points of the lower branch. In the case of $U = 1.481$ V, shown in Fig. 11(d), the amplitude of the current oscillation increases exponentially at first and after passing a certain threshold value quickly evolves into the large oscillations of the upper branch. The inset shows the transition region and indicates that the small charge fronts grow into mature ones. The rate λ can also be fitted and now it is positive. The resulting λ versus U is plotted in Fig. 11(e), showing a linear scaling. This clearly indicates that the bifurcation at A_l is a subcritical Hopf bifurcation. Supercritical Hopf bifurcations in different SL models have been found by Patra *et al.*[42] and by Hizanidis *et al.*[43] at low contact conductivity with no shunt. Here we can also see that the time scales have the following relationship: $\tau_b \ll 1/f_{1,2} \ll 1/\lambda$.

It is likely that the bifurcation scenario at A_u in Fig. 9(b) is a saddle-node bifurcation which is probably caused by the collision of the stable limit cycle and the unstable limit cycle that arises from the subcritical Hopf bifurcation at A_l. In Fig. 12(c), the power spectrum of the limit cycle ($U = 1.4997$ V) and the power spectrum of the transient oscillation at $U = 1.499\,85$ V—which exceeds the saddle-node bifurcation value U_{A_u}—are almost identical. This rules out a subcritical torus bifurcation. Then we start the system from a configuration corresponding to the steady oscillation at $U = 1.46$ V but for voltages just above U_{A_u} where there are no limit cycle states, so it eventually reaches the lower branch. Figure 12(a) shows this process at $U = 1.499\,85$ V. After a short time interval of about 1 μs, the oscillation amplitude $A(t)$ enters a regime of transient oscillations and after a relatively long time T, it suddenly exits this region and reaches a steady state. This process looks like a reverse process of Fig. 11(d). Figure 12(b) shows the decay of the CALs and CDLs. If we choose the critical value to be 1.499 791 V, then the slope in Fig. 12(d) is −0.5. This means that $T \propto \frac{1}{\sqrt{U - U_{A_u}}}$, consistent with a system that undergoes a saddle-node bifurcation of limit cycles.[44]

The bifurcation at point B is at $a = 1.00 \times 10^{-5}$ (Fig. 13). For $U \lesssim 2.305$ V, the system oscillates. At first, there is a single CAL in the SL and a dipole is injected from the emitter. The CAL and dipole all move into the SL. The leading CDL moves about twice as fast as the two CALs (Ref. 45) and when it catches up with the original CAL, they annihilate. The CAL of the dipole continues to move forward until it reaches the position of the original CAL and stays there for a certain period of time waiting for another round of dipole injection. Such a bifurcation of a stationary domain state has been reported before by Hizanidis *et al.*[46] for a one-dimensional superlattice model without shunt at higher contact conductivity. The time needed for a dipole to be injected is called the activation time and the time needed to return from the excited state to the fixed point is called the excursion time.[46] As the applied voltage U approaches the boundary, the activation time becomes longer and longer. Taking the critical value $U_{\mathrm{crit}B}$ of voltage to be 2.304 41 V and plotting the frequency of oscillation versus $U - U_{\mathrm{crit}B}$, we find the frequency obeys the square-root law which is the characteristic scaling law for the saddle-node infinite period bifurcation (SNIPER),[46] which is a global bifurcation of a limit cycle.

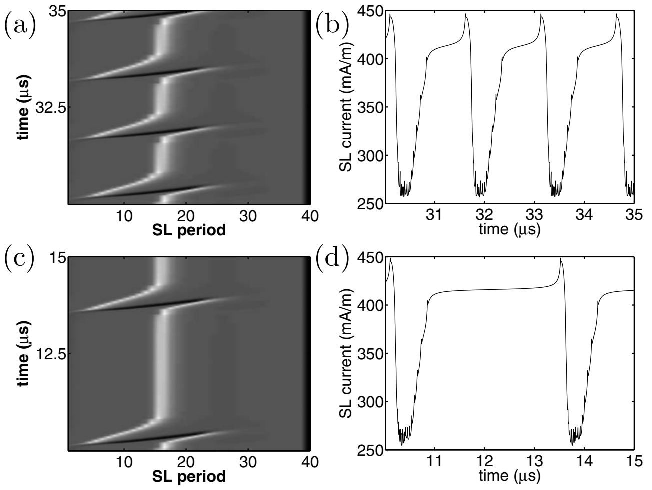

FIG. 13. Bifurcation scenario at point B of Fig. 9: [(a) and (c)] charge density distributions vs time; [(b) and (d)] SL current J_{SL} for $U = 2.3$ V (upper panel) and $U = 2.304$ V (lower panel), respectively, with $a = 1.00 \times 10^{-5}$, $\sigma = 0.04$ $(\Omega\ \mathrm{m})^{-1}$.

Inside the oscillatory region in the a-U parameter space [Fig. 9(a)], we also find regimes of chaos. We still use $a = 1.00 \times 10^{-3}$. As the voltage U decreases inside the oscillatory region, the oscillation shown in Fig. 10 involves a larger part of the SL and the CAL near the emitter becomes less and less prominent until these moving dipoles cover almost all the SL shown Figs. 14(a) and 14(b) at $U = 1.2$ and 1.0 V. Further decrease in the voltage causes the disappearance of the static CAL and the dipoles either annihilate inside the SL

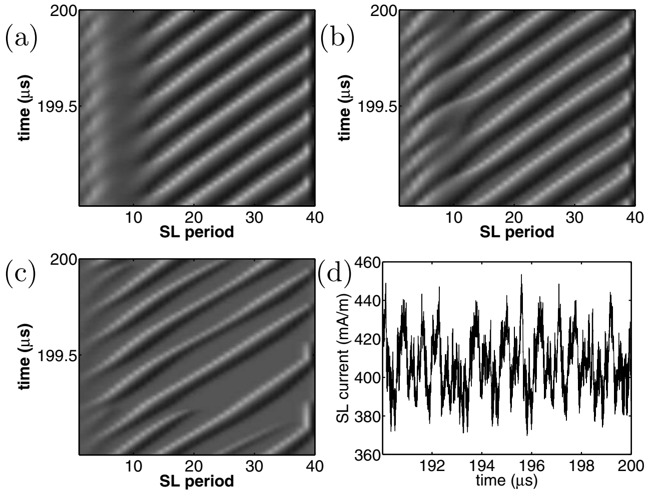

FIG. 14. Charge density distribution vs time for $a = 1.00 \times 10^{-3}$, $\sigma = 0.04$ $(\Omega\ \mathrm{m})^{-1}$ at (a) $U = 1.2$ V, (b) $U = 1$ V, and (c) $U = 0.5$ V. (d) SL current at $U = 0.5$ V.

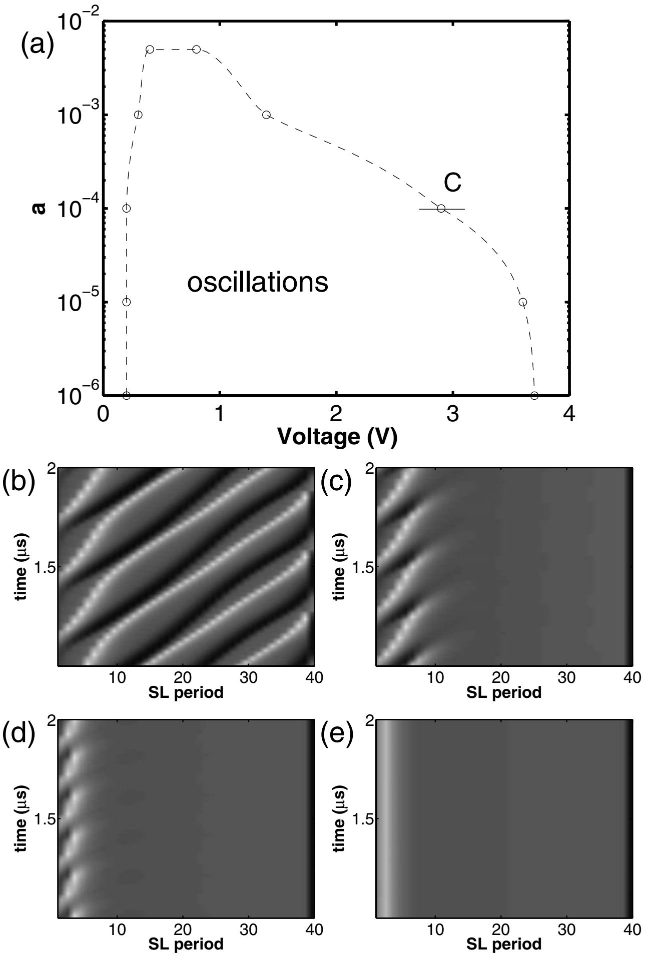

FIG. 15. (a) Bifurcation diagram for σ=0.016 $(\Omega\ \mathrm{m})^{-1}$. Charge density distribution vs time near bifurcation point C, a=1.00 $\times 10^{-4}$ at (b) U=1.6 V, (c) U=2.1 V, (d) U=2.7 V, and (e) U =3.0 V.

or reach and disappear at the collector, shown in Fig. 14(c) for U=0.5 V. Similar chaotic behavior has also been found in SLs without a shunt.[45] These complicated and apparently chaotic oscillations are found at many points in the oscillatory regime of Fig. 9(a).

In the regime of the stable states between $a \approx 6\times 10^{-3}$ and 7×10^{-6} [cf. the right-hand region of Fig. 9(a)], the SL usually has a static CAL either inside the SL (for low a) or attached to the emitter (for high a) and there is a small static CDL to the right of this CAL. This means that the overall field profile is nearly uniform for larger a ($\gtrsim 6\times 10^{-3}$), but static field domains form as a decreases.

B. Dynamical behavior for small contact conductivity

The bifurcation scenario for lower contact conductivity σ is simpler than for the high σ case. Figure 15 shows the bifurcation diagram for σ=0.016 $\Omega\ \mathrm{m}^{-1}$. This value of σ corresponds to current self-oscillation in the SL when there is no shunt.[32] The parameter space is again divided into an oscillatory regime and a stable stationary regime. The oscillatory regime starts at about the same value of a as the high σ case, i.e., $a \approx 6\times 10^{-3}$. However, this oscillatory region does not have a lower bound. This is because without the shunt the SL still exhibits oscillations.

The different behaviors at a=1.00$\times 10^{-4}$ are shown in Fig. 15. As the voltage is deep inside the oscillatory region, dipoles are periodically injected into the SL and travel through the entire SL [Fig. 15(b)]. As voltage increases, the distance that the dipoles travel becomes shorter and the CAL and CDL annihilate near the emitter [Fig. 15(c)]. Similar behaviors have been found in a SL model without shunt.[45] As the voltage approaches the boundary, the CDL becomes less and less prominent and the length that the CALs travel becomes even shorter. After the voltage crosses the boundary, the CALs become static. The bifurcation scenario is similar to point A, described in Sec. V A, where there is bistability between oscillatory and steady states. The bifurcation scenarios at other points on the right-hand boundary of the oscillatory region appear to be similar to that at point C.

C. Dynamical behavior vs shunt conductivity parameter *b*

The above discussion focuses only on varying the connectivity parameter a with a shunt of high conductance. It is also possible to change other parameters of the shunt, such as the conductivity parameter b in the shunt. A bifurcation diagram can be plotted for b versus U with fixed a=1.00 and δ_x =200 nm, and it is similar to that shown in Fig. 9, with an oscillatory regime between $b \approx 4.5\times 10^{-8}$ and 4.5×10^{-7}. Another possible control parameter is the width of the shunt. Simulation shows that only when the width of the shunt is narrower than about 1×10^{-4} nm, which is unrealistically small, the SL starts to have oscillation. The oscillatory region for a in Figs. 9 and 15 is almost not affected when b and δ_x are above certain values so that the current between the shunt and the SL can always be supported by the shunt. In reality, δ_x and b should be kept as low as possible to reduce the power dissipated in the shunt and minimize heat production.

VI. CONCLUSIONS

We have theoretically studied the effect of a shunting side layer parallel to a semiconductor superlattice and find that such a structure can have an almost uniform electric field over the entire structure even when biased in the negative differential conductivity (NDC) region. However, even for a shunt with high conductivity and strong connection to the SL, the field in the SL can be stabilized only for structures with relatively small lateral extent. As the lateral size L_x becomes larger, the lateral current in the quantum well loses the ability to deplete the extra current coming from the emitter and the field becomes nonuniform. For a sufficiently thin SL whose lateral dynamics is uniform, the connection between the shunt and the SL and the conductivity of the shunt determines the dynamics in the SL. We have also established the bifurcation diagrams for SLs for different values of the shunt parameters and identified the presence of both local (Hopf) and global (SNIPER) bifurcations.

Although the microscopic nature of electronic transport in weakly coupled SLs is different than for strongly coupled

SLs, the NDC property is known to produce similar dynamics in both types of structures when they are not shunted. Thus, it seems plausible that for suitable shunt connectivity and SL lateral width that strongly coupled SL might also be stabilized with a shunting side layer. This could enable the realization of a SL-based terahertz oscillator.

ACKNOWLEDGMENTS

This work was supported in part by NSF under Grant No. DMR-0804232, by IRCSET, by SFI, and by DFG under Grant No. Sfb 555.

APPENDIX: NUMERICAL METHOD

In order to implement the implicit method, the dynamical variables, i.e., the electron densities $n_m(x)$, should be computed from the system [Eqs. (3) and (13)]. However, the $n_m(x)$ are deeply buried in these equations, where the currents depend on the field that relates to $n_m(x)$ by solving Poisson equation [Eq. (7)]. So instead of solving for $n_m(x)$ directly, we use the semi-implicit Euler method and numerically calculate the Jacobian matrix that is needed for this method. The procedure is as follows: after discretization of the space, the quantities of potential and charge density are placed on the grid. The fields and currents (also the charge density that is needed to calculate the currents) are placed on a staggered grid. Knowing the charge density distribution, the potential is determined by the Poisson equation using a method described in Ref. 33. After that, the currents to each grid point are calculated from the electric fields which are immediately obtained from the potential [cf. Eqs. (10) and (16)]. Then the charge densities are iterated one step forward in time as

$$e\mathbf{n}' = e\mathbf{n} + dt\mathbf{J}(\mathbf{n}'), \tag{A1}$$

where $\mathbf{n}=(n_{11},n_{12},\ldots,n_{21},n_{22},\ldots)^T$ is the vector whose components are the charge densities on each grid point. The first subscript denotes the SL period number and the second one is the grid point index in the x direction. The vector current $\mathbf{J}$ is the total current flow into or out of each grid point. $\mathbf{n}'$ is the new charge density configuration after time step dt. Since we are using the implicit method, $\mathbf{J}$ must depend on the future charge density configuration instead of the old one. We linearize the equations

$$\mathbf{n}' = \mathbf{n} + \frac{dt}{e}\left[\mathbf{J}(\mathbf{n}) + \left.\frac{\partial \mathbf{J}}{\partial \mathbf{n}}\right|_{\mathbf{n}} \cdot (\mathbf{n}' - \mathbf{n})\right], \tag{A2}$$

where $\partial J/\partial n$ is the Jacobian matrix. Rearranging this equation yields

$$\mathbf{n}' = \mathbf{n} + \frac{dt}{e}\left[1 - dt\frac{\partial \mathbf{J}}{\partial \mathbf{n}}\right]^{-1} \cdot \mathbf{J}(\mathbf{n}). \tag{A3}$$

We mentioned that the currents do not depend on the charge densities explicitly. So to calculate the Jacobian matrix, we first calculate $\mathbf{J}(\mathbf{n})$, then slightly change the charge density at one grid point to $n_{ij}+\delta n_{ij}$, and calculate the currents $\mathbf{J}'$ based on this charge configuration. Then one row of the Jacobian matrix is immediately obtained by $[\mathbf{J}'-\mathbf{J}(\mathbf{n})]/\delta n_{ij}$.

To solve Eq. (A3), we do not invert the matrix. Instead, we write it as

$$\frac{dt\mathbf{J}(\mathbf{n})}{e} = \left[1 - dt\frac{\partial \mathbf{J}}{\partial \mathbf{n}}\right] \cdot (\mathbf{n}' - \mathbf{n}). \tag{A4}$$

Then we solve this set of linear equations by Gauss elimination.

---

[1] L. Esaki and R. Tsu, IBM J. Res. Dev. **14**, 61 (1970).

[2] F. Bloch, Z. Phys. **52**, 555 (1928).

[3] C. Zener, Proc. R. Soc. London, Ser. A **145**, 523 (1934).

[4] S. A. Ktitorov, G. S. Simin, and V. Y. Sindalovskii, Sov. Phys. Solid State **13**, 1872 (1972).

[5] J. Feldmann, K. Leo, J. Shah, D. A. B. Miller, J. E. Cunningham, T. Meier, G. von Plessen, A. Schulze, P. Thomas, and S. Schmitt-Rink, Phys. Rev. B **46**, 7252 (1992).

[6] E. E. Mendez, F. Agulló-Rueda, and J. M. Hong, Phys. Rev. Lett. **60**, 2426 (1988).

[7] T. Yajima and Y. Taira, J. Phys. Soc. Jpn. **47**, 1620 (1979).

[8] K. Leo, J. Shah, E. O. Göbel, T. C. Damen, S. Schmitt-Rink, W. Schäfer, and K. Köhler, Phys. Rev. Lett. **66**, 201 (1991).

[9] C. Waschke, H. G. Roskos, R. Schwedler, K. Leo, H. Kurz, and K. Kohler, Phys. Rev. Lett. **70**, 3319 (1993).

[10] R. Martini, G. Klose, H. G. Roskos, H. Kurz, H. T. Grahn, and R. Hey, Phys. Rev. B **54**, R14325 (1996).

[11] J. B. Gunn, Solid State Commun. **1**, 88 (1963).

[12] E. Schomburg, K. Hofbeck, J. Grenzer, T. Blomeier, A. A. Ignatov, K. F. Renk, D. G. Pavel'ev, Y. Koschurinov, V. Ustinov, A. Zhukov, S. Ivanov, and P. S. Kop'ev, Appl. Phys. Lett. **71**, 401 (1997).

[13] B. S. Williams, S. Kumar, Q. Hu, and J. L. Reno, Opt. Express **13**, 3331 (2005).

[14] H. Willenberg, G. H. Dohler, and J. Faist, Phys. Rev. B **67**, 085315 (2003).

[15] A. G. Davies, E. H. Linfield, and M. Pepper, Philos. Trans. R. Soc. London, Ser. A **362**, 197 (2004), special issue terahertz gap.

[16] T. Hyart, K. N. Alekseev, and E. V. Thuneberg, Phys. Rev. B **77**, 165330 (2008).

[17] H. Kroemer, arXiv:cond-mat/0009311 (unpublished).

[18] T. Hyart, N. V. Alexeeva, J. Mattas, and K. N. Alekseev, arXiv:0812.4046 (unpublished).

[19] T. Hyart, N. V. Alexeeva, A. Leppnen, and K. N. Alekseev, Appl. Phys. Lett. **89**, 132105 (2006).

[20] T. Hyart, A. V. Shorokhov, and K. N. Alekseev, Phys. Rev. Lett. **98**, 220404 (2007).

[21] P. G. Savvidis, B. Kolasa, G. Lee, and S. J. Allen, Phys. Rev. Lett. **92**, 196802 (2004).

[22] M. Bao and K. L. Wang, IEEE Trans. Electron Devices **53**, 2564 (2006).

[23] J. T. Wallmark, L. Varettoni, and H. Ur, IEEE Trans. Electron Devices **10**, 359 (1963).

[24] E. Daniel, B. Gilbert, J. Scott, and S. Allen, IEEE Trans. Electron Devices **50**, 2434 (2003).

[25] L. L. Bonilla and H. T. Grahn, Rep. Prog. Phys. **68**, 577 (2005).

[26] T. Feil, H.-P. Tranitz, M. Reinwald, and W. Wegscheider, Appl. Phys. Lett. **87**, 212112 (2005).

[27] A. Wacker, Phys. Rep. **357**, 1 (2002).

[28] E. Schomburg, K. Hofbeck, R. Scheuerer, M. Haeussler, K. F. Renk, A.-K. Jappsen, A. Amann, A. Wacker, E. Schöll, D. G. Pavel'ev, and Y. Koschurinov, Phys. Rev. B **65**, 155320 (2002).

[29] R. Scheuerer, E. Schomburg, K. F. Renk, A. Wacker, and E. Schöll, Appl. Phys. Lett. **81**, 1515 (2002).

[30] A.-K. Jappsen, A. Amann, A. Wacker, E. Schöll, and E. Schomburg, J. Appl. Phys. **92**, 3137 (2002).

[31] E. Schöll, *Nonlinear Spatio-Temporal Dynamics and Chaos in Semiconductors*, Nonlinear Science Series Vol. 10 (Cambridge University Press, Cambridge, 2001).

[32] H. Xu and S. W. Teitsworth, Phys. Rev. B **76**, 235302 (2007).

[33] A. Amann and E. Schöll, Phys. Rev. B **72**, 165319 (2005).

[34] V. Cheianov, P. Rodin, and E. Schöll, Phys. Rev. B **62**, 9966 (2000).

[35] L. Pfeiffer, K. W. West, H. L. Stormer, J. P. Eisenstein, K. W. Baldwin, and D. Gershoni, Appl. Phys. Lett. **56**, 1697 (1990).

[36] W. Wegscheider, L. Pfeiffer, and K. West, Appl. Phys. Lett. **65**, 2510 (1994).

[37] M. Rogozia, S. W. Teitsworth, H. T. Grahn, and K. H. Ploog, Phys. Rev. B **64**, 041308(R) (2001).

[38] K. J. Luo, H. T. Grahn, and K. H. Ploog, Phys. Rev. B **57**, R6838 (1998).

[39] A. Amann, A. Wacker, and E. Schöll, Physica B **314**, 404 (2002).

[40] A. Amann, J. Schlesner, A. Wacker, and E. Schöll, Phys. Rev. B **65**, 193313 (2002).

[41] H. Xu (unpublished).

[42] M. Patra, G. Schwarz, and E. Schöll, Phys. Rev. B **57**, 1824 (1998).

[43] J. Hizanidis, A. G. Balanov, A. Amann, and E. Schöll, Int. J. Bifurcation Chaos Appl. Sci. Eng. **16**, 1701 (2006).

[44] S. H. Strogatz, *Nonlinear Dynamics and Chaos: With Applications to Physics, Biology, Chemistry and Engineering* (Westview, New York, 2001).

[45] A. Amann and E. Schöll, J. Stat. Phys. **119**, 1069 (2005).

[46] J. Hizanidis, A. Balanov, A. Amann, and E. Schöll, Phys. Rev. Lett. **96**, 244104 (2006).